Journal of Materials Chemistry A

Accepted Manuscript

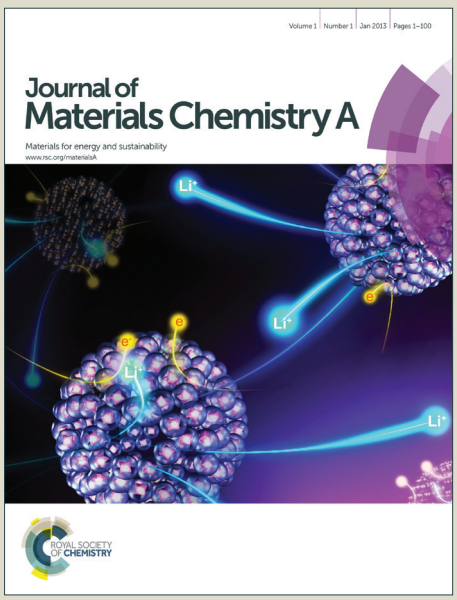

ROYAL SOCIETY OF CHEMISTRY

www.rsc.org/materialsA

All solid state, high performance supercapacitor using Zinc Manganite embedded Graphene nanoribbons

Preety Ahuja, Raj Kishore Sharma* and Gurmeet Singh

Department of Chemistry, University of Delhi, Delhi 110007, INDIA

Abstract

Fabrication of flexible supercapacitors involves challenging task of preparing flexible electrodes with large capacitance and robust mechanical strength. In this work, we demonstrate the formulation of high performance all solid state, flexible supercapacitor by using zinc manganite embedded graphene nanoribbons ($ZnMn_2O_4$/GNR) as electrode and gel polymer membrane as electrolyte. In situ availability of graphene oxide nanoribbon (GONR), leads to uniform dispersion of $ZnMn_2O_4$ nanosphere (~7 nm) that consequently result in enhanced electrolyte ions transport. Fabricated supercapacitor, $ZnMn_2O_4$/GNR||$ZnMn_2O_4$/GNR has been optimized with maximum 2.7 V operating cell potential. It delivers energy density ~37 Wh Kg^{-1} and power density ~30 kW kg^{-1} at 1.25 Ag^{-1} with good cycling stability over 4000 cycles. High diffusion coefficient and short relaxation time 0.34 μs (at 75 ^oC) are indication of its high performance and stability at elevated temperature. The superior flexibility and durability of the supercapacitor cell are evident of their performance stability over consecutive GCD cycles under harsh conditions.

Keywords

Zinc Manganite, graphene nanoribbon, flexible supercapacitor, diffusion coefficient.

Corresponding Author: Dr. Raj K. Sharma,
Email: drrajksharma@yahoo.co.in, rajksharma@chemistry.du.ac.in, phone 91 11 27777716

1. Introduction

In modern era, growing energy requirement lead to production of energy and power in an environmental benign manner for emerging flexible and wearable electronic devices [1, 2]. Supercapacitors, an important energy storage device, provide peak power pulses with high power density than batteries and store more energy than conventional capacitors. They can complement other energy storage devices such as batteries and fuel cells owing to their long cycling life and rapid charging and discharging at high current densities [3, 4]. Supercapacitors have profound applications providing fast bursts of energy or as backup power sources in electric vehicles [5]. Charge storage mechanism in supercapacitors is based on two; the double layer formation at electrode/electrolyte interface (EDLC) and pseudocapacitors where charge storage occurs via faradic processes involving electron transfer reactions [6].

EDLC utilizes electrostatic accumulation of charges at the electrode/electrolyte interface and the resulting low specific capacitance limit the applications requiring high energy density. Considerable effort has been devoted to the development of new electrode materials with improved performance. Graphene based materials have attracted considerable attention in supercapacitor electrodes owing to their outstanding electrical and physiochemical properties [7]. Conversely, they undergo agglomeration through van der Waals interaction during graphene preparation and electrode formation processes ensuing in loss of electrochemical performance [8].

Laterally constraining the carriers in quasi one dimensional system, Graphene nanoribbon (GNR) provides an extremely high surface area, excellent conductivity and high mechanical strength for applications in supercapacitor [9-11]. Moreover, incorporation of electroactive materials as spacers significantly improves the overall performance of GNR

based supercapacitors [12]. Efforts have been devoted for fabricating nanocomposites of transition metal oxides and graphene nanoribbons such as GNR/SnO_2 which has profound applications in Li ion batteries [13]. These composites are expected to show enhanced performance in supercapacitors due to accommodation of volume change during charge/discharge, high ionic accessibility and balanced electronic and ionic conduction that consequently reduce the diffusion length of the electrolytic ions [14].

Among various electro-active materials, spinel transition metal oxides are attracting great attention for potential applications in supercapacitors because of their enhanced characteristic over single material [15, 16]. Spinel structures, AB_2O_4 are regarded as mixed valence oxide with richer redox chemistry than the two single component oxides due to combined contribution from individual oxides [17, 18]. We have recently shown the superior performance of Nickel manganite supercapacitor electrodes [19]. $ZnMn_2O_4$ (Zinc manganite) has been widely used in the fields of magnetic materials, electro-catalysts and Li-ion batteries [20-22]. However to the author knowledge, there are no reports on fabrication and electrochemical performance of flexible solid state supercapacitor based on $ZnMn_2O_4$/GNR composite to the best of our knowledge.

Regardless of valuable research, performance of the supercapacitor device is still below the expectations. This may be due to less attention towards the cell voltage which is a crucial factor for attaining high energy and power density [23]. Fabricating asymmetric supercapacitors in aqueous electrolytes can widen the operating potential range up to 2 V but with typically low energy density [24]. However, for safety contemplation, solid state electrolytes are superior compared to liquid counterpart [25]. In this perspective, ionic liquid based gel polymer electrolyte is utilized in fabricating solid state electrochemical devices [26, 27].

In the present article, we for the first time report the synthesis of $ZnMn_2O_4$/GNR by microemulsion method and in situ reduction of GONR. The $ZnMn_2O_4$/GNR composite supercapacitor electrode during electrochemical evaluation indicated that fabricated supercapacitor $ZnMn_2O_4$/GNR||$ZnMn_2O_4$/GNR can be cycled reversibly in 0 to 2.7 V and delivers high energy and power density (37 Wh Kg^{-1} and 30 kW Kg^{-1}). It exhibits long term stability even after 4000 galvanic charge/discharge cycles.

2. Experimental

Zinc chloride ($ZnCl_2.6H_2O$), Manganese chloride ($MnCl_2.4H_2O$), Sodium hydroxide (NaOH), Sodium sulphate (Na_2SO_4), acetone, isopropyl alcohol (IPA) and isooctane were purchased from Merck. Sodium sulphosuccinate (AOT) was used as surfactant (supplied by Alfa Aesar). MWCNT were purchased from Shenzhen Nanotech Port, Co. Limited, China, diameter 10–20 nm and length ~1 μm. Poly(vinylidenefluoride hexafluoropropylene) (PVdF-HFP), 1-butyl-3-methylimidazolium tetrafluoroborate [BMIM][BF_4] ionic liquid and Perfluorinated ion exchange resin (Nafion) were purchased from Sigma Aldrich.

2.1 Synthesis of GONR

Graphene oxide nanoribbons were synthesized by longitudinal unzipping of carbon nanotubes [28]. Briefly, MWCNT was added in conc. H_2SO_4 (98%) + conc. H_3PO_4 solution and stirred for 30 min. Then, $KMnO_4$ was added gradually to H_2SO_4/H_3PO_4 dispersed MWCNT. The solution was heated for 2 hr at 65^oC and allowed to cool naturally. For extracting GONR from reaction mixture, 400 ml ice containing 30% H_2O_2 solution was added and dark brown precipitate settled at the bottom. This was repeatedly washed with ethanol and DI water. The product was filtered via 0.45 μm PTFE membrane and filtered GONR was kept in vacuum desiccators.

2.2 Synthesis of $ZnMn_2O_4$/GNR

AOT (8 g) was mixed with 80 ml of isooctane and stirred for 2 hr to get a transparent solution [29]. Resulting solution was divided into 4 parts and aqueous solutions of 0.6 M $MnCl_2$, 0.3 M $ZnCl_2$, 2 M NaOH and 20 wt % GONR (dispersed in water) were added respectively. Each of these microemulsions was stirred for 3 hr and mixed sequentially in a reaction vessel under stirring. Excess volume of IPA was then added to break these microemulsions and the precipitate of $ZnMn_2O_4$ embedded graphene nanoribbon ($ZnMn_2O_4$/GNR) was then collected. Obtained product was washed several times with IPA and deionized water and dried at 80^oC in vacuum oven. The percentage composition of $ZnMn_2O_4$ in the yield of $ZnMn_2O_4$/GNR composite was found to be approximately 70 wt %.

2.3 Preparation of electrode

$ZnMn_2O_4$/GNR (30 mg) was added in solution of 5 wt% Nafion in IPA. This mixture was sonicated for 1 hr and spray deposited over 1 cm^2 of the polished graphite plates. After spray deposition, the film was dried at 80^oC in air and the material loading was found to be approximately 0.4 mg/cm^2.

2.4 Preparation of gel polymer electrolyte

Gel polymer electrolyte was fabricated as described earlier by G. P. Pandey et al [30]. Briefly, host polymer [PVdF-HFP] was dissolved in acetone and then Ionic liquid [BMIM][BF_4] was mixed with [PVdF-HFP]+acetone solution and stirred for 12 h. The weight ratio of ionic liquid to polymer was kept 4:1. As obtained viscous solution was cast on glass petridish and kept untouched for 3 days to allow acetone to evaporate resulting in the formation of transparent and free-standing gel electrolyte. The electrolyte film was stored in inert atmosphere to avoid moisture adsorption.

2.5 Assembly of supercapacitor, $ZnMn_2O_4$/GNR||$ZnMn_2O_4$/GNR

Gel polymer electrolyte membrane, was cut to 1cm^2, placed between two similar $ZnMn_2O_4$/GNR electrodes and gently pressed to form all solid state supercapacitor. The thickness of gel polymer electrolyte was kept same for all the cells.

2.6 Physical and Electrochemical Characterization

High resolution transmission electron microscopy (HRTEM) and Selected Area Electron Diffraction (SAED) was conducted on Phillips Technai T-300 microscope. Zeiss Ultra 55 field emission scanning electron microscope (FESEM) was used for surface analysis. Powder X-Ray Diffraction (XRD) measurements were performed with a Bruker D8 Advance X-ray diffractometer. Powder samples were analyzed by Raman Spectroscopy on Renishaw inVia Raman microscope. FTIR spectra of powder samples in KBr pellet form were recorded on a Perkin-Elmer FT-IR spectrum BX spectrometer. Electrochemical tests were performed with CHI 604D electrochemical analyzer. Charge/discharge characteristics of the supercapacitor cell were evaluated at different current density using an Arbin instrument (model: BT2000, USA). The specific capacitance was calculated from galvanostatic charge discharge curve according to the following equation [31]:

$$C = \frac{I\Delta t}{m\Delta V}$$

where I is the current, $\Delta V/\Delta t$ is the change in potential with time and m is the mass of active material on two electrodes. The energy density (E in Wh Kg^{-1}) and power density (P in kW Kg^{-1}) were expressed as

$$E = \frac{1}{2\times 3.6} CV^2$$

$$P = \frac{V^2}{4mR}$$

where C is measured device capacitance, m is the mass of active material of two electrodes, V is the operating potential range and R is the equivalent series resistance calculated from IR drop in galvanostatic discharge curve.

3. Results and Discussion

3.1 Structural Analysis

Synthesis and structural characterisation of GONR is discussed in our earlier communication [28]. The present work discusses the reduction of GONR, formation and uniform dispersion of $ZnMn_2O_4$ over GNR. Large area distribution of $ZnMn_2O_4$/GNR nanocomposite shown in the TEM image of Fig. 1a. Demonstrate that that the GNR ribbons are uniformly covered by $ZnMn_2O_4$ nanoparticles. Figure 1b demonstrate that $ZnMn_2O_4$ crystallizes are monodispersed and are spherical in shape. Inset (Figure 1b) endosre the monodispersion of $ZnMn_2O_4$ nanoparticles (dia. ~20 nm) and uniform distribution all over the GNR. Unique set of fringes can be explicitly identified with fringe width 0.27 nm for (103) plane, 0.24 nm for (211) and 0.15 nm for (224) (Figure 1c). Spotty SAED pattern of $ZnMn_2O_4$/GNR in Figure 1d reveals crystalline nature of $ZnMn_2O_4$. Characteristic lattice planes (112), (211), (224) and (103) are indexed to spinel $ZnMn_2O_4$ (JCPDS No. 77-0470). SEM micrograph of the $ZnMn_2O_4$/GNR composite in Figure 1e shows homogeneous distribution of $ZnMn_2O_4$/GNR without any phase sepration. The rough morphology indicate the high acessibility of the material by electrolytic ions. Figure 1f shows XRD pattern of GONR and $ZnMn_2O_4$/GNR. GONR shows a prominent peak at 10^o indicating highly oxidized GONR [32]. Three peaks present in $ZnMn_2O_4$/GNR corresponds to (103), (211) and (321) planes of $ZnMn_2O_4$ which are in correlation with SAED pattern. However, obvious

peak of GNR at 24° is also not observed indicating disordered stacking of GNR in presence of $ZnMn_2O_4$ nanoparticles [33, 34]. From the detailed analysis, it is confirmed that this material is crystalline tetragonal $ZnMn_2O_4$ with cell parameters a= 5.72Å and c= 9.74Å.

Reduction of GONR in $ZnMn_2O_4$/GNR composite is scrutinized by Raman and FTIR analysis. Raman spectra of $ZnMn_2O_4$/GNR and GONR in Figure 2a are mainly characterized by two features: G band and D band. G band results from vibrations of sp^2 C atoms and D band arises from disorderness or defect density in crystal [35]. Intensity ratio of D and G band, I_D/I_G is used to quantify the relative content of defect and sp^2 domain size. I_D/I_G ratio of GONR is found to be ~1.09 (Figure 2a) whereas $ZnMn_2O_4$/GNR exhibits I_D/I_G ratio ~1.23 indicating decrease in sp^2 domains and the removal of oxygen functionalities in GONR [36, 37]. Moreover, this increased I_D/I_G implies increase in disorderness with binding of $ZnMn_2O_4$ nano-spheres via oxygen containing moieties present on GONR. Moreover, four Raman active modes of the spinel $ZnMn_2O_4$ are also observed at 174, 337, 400 and 649 cm^{-1} (inset) which belongs to Mn-O and Zn-O breathing vibrations [38].

Absorption bands at 1059, 1176 and 1396 cm^{-1} in FTIR spectra of GONR are ascribed to C-O stretching of alkoxide, epoxide and alkoxy groups respectively (Figure 2b). Characteristic bands at 1601 and 1712 cm^{-1} reveals the presence of C=C and C=O moieties respectively [39]. Reduction in intensity of C=O stretching absorption band at 1712 cm^{-1} in $ZnMn_2O_4$/GNR confirms deoxygenation of GONR supporting Raman analysis. Peaks in the lower frequency region can be assigned to Mn-O and Zn-O stretching vibration in $ZnMn_2O_4$ [40].

3.2 Electrochemical Analysis

Electrochemical performance of $ZnMn_2O_4$/GNR for all solid state flexible supercapacitor is analyzed by Cyclic Voltammetry (CV), Electrochemical Impedance

Spectroscopy (EIS) and Galvanostatic charge discharge (GCD) measurements. Figure 3a shows CV of supercapacitor cell, $ZnMn_2O_4$/GNR||$ZnMn_2O_4$/GNR with inset illustrating specific capacitance variation in different potential range at 25 mVs^{-1}. Interestingly, it exhibited capacitive behaviour with nearly rectangular voltammogram, even in a wider potential range 2.7 V. Deviation from the ideal rectangular profile is attributed to lesser ionic conductivity of the electrolyte at room temperature. With further increase in potential range, sharp increment in current is observed at the extreme potential (not shown here). The increase in anodic and cathodic current at high voltages is due to the electro oxidation of BF_4^- to BF_3 and fluorocarbons with electro reduction of imidazolium ring in the cation [41]. Therefore, we chose potential range 0 to 2.7 V to further investigate the electrochemical performance of the supercapacitor cell. Evidently, the area covered in the CV curve of $ZnMn_2O_4$/GNR is dramatically enhanced from that of $ZnMn_2O_4$ and GNR (Figure 3b). This enhancement is attributed to the presence of GNRs, which greatly shortened the ion diffusion path ensuring high utilization of surface pseudocapacitive reactions with the beneficial EDLC and conductivity effects of underlying GNR. Figure 3c shows CV of $ZnMn_2O_4$/GNR||$ZnMn_2O_4$/GNR at different scan rates revealing nearly rectangular shaped voltammograms. Absence of redox peaks in voltammogram implies pseudoconstant rate of charging and discharging over whole voltammetric cycle [42]. As the scan rate increases, the shape of the curve deviates because of overpotential [43]. It is observed that the specific capacitance of the cell, $ZnMn_2O_4$/GNR||$ZnMn_2O_4$/GNR shows decrement with the increase in scan rate reflecting reduced accessible surface area by the electrolyte at higher scan rates (inset).

As a power source for electric vehicles, supercapacitors are required to operate at higher temperature (~75^oC). Figure 3d shows CV of $ZnMn_2O_4$/GNR||$ZnMn_2O_4$/GNR cell (80mVs^{-1}) at different temperatures. The increase in current at high temperature is due to

increase in electrolyte conductivity as well as electrochemically active electrode/electrolyte interfaces [44]. These interfacial processes at higher temperature are further examined by EIS. Figure 4a shows Nyquist plot at 25^{o}C & 75^{o}C in frequency range 0.001Hz-1MHz. Semicircle in high frequency region corresponds to charge transfer resistance (R_{CT}) 0.9 ohm and 1.1 ohm at 25 and 75^{o}C respectively. Solution resistance (R_S) are 11.1 and 7.9 ohm at 25^{o}C and 75^{o}C respectively which decreases with increase in temperature as shown in the inset. The series resistance (R_S + R_{CT}) is responsible for ohmic drop of the cell and hence lower cell resistance is suitable for higher power density. Series resistance of $ZnMn_2O_4$/GNR||$ZnMn_2O_4$/GNR is found to be 12 and 10 ohm at 25^{o} and 75^{o}C respectively which is much lower than that of graphene based supercapacitors (16 ohm) [45]. At 75 ^{o}C, lower frequency region incline more towards imaginary axis illustrating improved capacitive performance at higher temperatures. The temperature increment has no major effect in low frequency region but magnified in high-mid frequency region which may arises from thermally activated ion's physical adsorption [46].

To explore the effect of increasing temperature on diffusion length of ions, impedance data was employed to determine the diffusion coefficient at 25^{o}C and 75^{o}C. The diffusion controlled regime [($\Delta Z_{im}/\Delta Z_{re}$~ 1) is observed to fall in the frequency range 8Hz - 0.8Hz [47, 48, 28]. In this frequency range, the diffusion coefficients calculated in accordance with our previous report at the respective temperatures, 25^{o}C and 75^{o}C and are found to be 1.4 X 10^{-7} and 2.5 X 10^{-7} cm^2s^{-1} respectively (Figure 4b). The higher value at 75^{o}C must be associated with fast and efficient ionic pathways due to the enhanced accessibility of ion adsorption-desorption at higher temperature.

Complex power analysis is required to determine the relaxation time which is a figure of merit of supercapacitor [49, 28]. Figure 4c shows variation of normalized active and reactive power with frequency which intersect at a point of maximum energy dissipation. The

frequency f at highest energy dissipation is capacitor response frequency which corresponds to the relaxation time of the supercapacitor and is found to be 0.65μs at 25°C. This ultra short relaxation time is much higher than the previously reported values of graphene based nanocomposites in solid state supercapacitor [41]. With increase in temperature, relaxation time decreases to 0.34 μs (Figure 4d) implying excellent discharge characteristics at higher temperature. Moreover, this lesser relaxation time is also associated with faster kinetics which is in correlation with higher diffusion coefficient at 75°C.

Figure 5a illustrates GCD curves of the supercapacitor, GNR‖GNR, $ZnMn_2O_4$‖$ZnMn_2O_4$ & $ZnMn_2O_4$/GNR‖$ZnMn_2O_4$/GNR in potential range of 0 to 2.7 V at 1.25 Ag^{-1}. The discharge counterpart of GNR‖GNR is relatively linear as compared to that of $ZnMn_2O_4$/GNR‖$ZnMn_2O_4$/GNR and $ZnMn_2O_4$‖$ZnMn_2O_4$ (dominating pseudocapacitance). This manifests the formation of EDL in GNR‖GNR. GCD curves of $ZnMn_2O_4$/GNR‖$ZnMn_2O_4$/GNR at different current densities are shown in Figure 5b. Slightly curved discharge counterparts in all GCD profiles indicate the dominating pseudocapacitive contribution in the system. The charge/discharge lines are approximately proportional to charge/discharge times implying fast current voltage response.

The excellent performance of the cell can be clearly understood by two important parameters i.e. energy and power density. Ragone plot (Figure 5c) reveals the variation of energy and power density at different current densities in GNR‖GNR, $ZnMn_2O_4$‖$ZnMn_2O_4$ and $ZnMn_2O_4$/GNR‖$ZnMn_2O_4$/GNR device. The cell exhibits higher energy density ~37 $WhKg^{-1}$ and power density ~30 kW Kg^{-1} at 1.25 Ag^{-1} which outperforms that of GNR‖GNR (13 Wh Kg^{-1}, 15 kW kg^{-1}) and earlier reported graphene based nanocomposites for solid state supercapacitors [50]. It still maintains an energy and power density ~9.9 $WhKg^{-1}$ and ~40 kW Kg^{-1} respectively at 6.25 Ag^{-1}.

Long term stability of the cell $ZnMn_2O_4$/GNR||$ZnMn_2O_4$/GNR is explored by employing consecutive GCD cycling at 2.5 Ag^{-1} as shown in Figure 5d. Inset shows overview of last cycles. It is observed that specific capacitance increases in the initial cycles followed by decrement during next 1500 cycles and steady performance in the subsequent cycles. The cell maintains 91% of the initial capacitance even after 4000 cycles endowing a long term stable material for high performance solid state supercapacitor.

More importantly, the electrode material fabricated on flexible graphite hold great potential for flexible energy storage systems. GCD cycling at 0.2 Ag^{-1} under different conditions (bending) shows steady performance ascertaining durability of the device under harsh conditions (Figure 6). Inset shows photograph of all solid state flexible supercapacitor under normal, twist and bent conditions. GCD curves under normal, twisted and bent condition (second inset) are similar indicating excellent performance as flexible energy storage device.

Several factors endow $ZnMn_2O_4$/GNR with superior and excellent electrochemical performance. Firstly, uniform dispersion of $ZnMn_2O_4$ nanoparticles on graphene nanoribbons provides highly accessible electrochemically active surface for exploiting the full spectrum of $ZnMn_2O_4$ pseudocapacitance and double layer capacitance of graphene nanoribbons. Secondly, wide operating potential range of the fabricated supercapacitor i.e. 2.7 V provides higher energy density which outperforms most of the present graphene based supercapacitors.

4. Conclusion

Uniformly dispersed $ZnMn_2O_4$ on graphene nanoribbons ($ZnMn_2O_4$/GNR) was successfully synthesized and characterized as electrode material for all solid state flexible supercapacitor. Fabricated supercapacitor, $ZnMn_2O_4$/GNR‖$ZnMn_2O_4$/GNR demonstrates excellent electrochemical performance in wide potential range 2.7 V. The specific

capacitance demonstrated linear dependence with increasing temperature which might be associated to high diffusion coefficient to 2.5 x 10^{-7} cm^2s^{-1} and low relaxation time to 0.34 μs at high temperature (75 ^oC). It delivers extremely high energy density ~37 Wh Kg^{-1} with power density ~30 $kWkg^{-1}$ at 1.25 Ag^{-1} and exhibits excellent cycling stability with 91% capacitive retention after 4000 cycles. Durability of all solid state supercapacitor under harsh conditions ascertains its great application potential to the fundamental research and technologies of flexible energy storage device.

Acknowledgements

Authors gratefully acknowledge the financial support through the R&D grant of Delhi University. PA acknowledges the Ph. D fellowship received from UGC. Financial support through SERB project (Grant No. SR/S1/ PC-31/2010) from DST, New Delhi is gratefully acknowledged.

References

1. L. Hu, H. Wu, F. L. Mantia, Y. Yang, Y. Cui, ACS Nano 2010, 4, 5843-5848.
2. B. G. Choi, S. J. Chang, H. W. Kang, C. P. Park, H. J. Kim, W. H. Hong, S. G. Lee, Y. S. Huh, Nanoscale 2012, 4, 4983-4988.
3. P. Simon, Y. Gogotsi, Nat. Mater. 2008, 7, 845-854.
4. G. P. Pandey, S. A. Hashmi, Electrochim. Acta 2013, 105, 333-341.
5. G. Zhang, X. W. Lou, Adv. Mater. 2013, 25, 976-979.
6. Y. J. Kang, H. Cheng, C. H. Han, W. Kim, Nanotechnology 2012, 23, 065401.
7. D. Chen, L. Tang, J. Li, Chem. Soc. Rev. 2010, 39, 3157-3180
8. M. S. Wu, Y. H. Fu, Carbon 2013, 60, 236-245.
9. M. Y. Han, B. Ozyilmaz, Y. B. Zhang, P. Kim, Phys. Rev. Lett. 2007, 98, 2068051-2068054-1-2068054-4.

10. O. Hod, V. Barone, J. E. Peralta, G. E. Scuseria, Nano Lett. 2007, 7, 2295-2299.

11. K. N. Kudin, ACS Nano 2008, 2, 516-522.

12. K. Zhang, L. L. Zhang, X. S. Zhao, J. S. Wu, Chem. Mater. 2010, 22, 1392.

13. J. Lin, Z. Peng, C. Xiang, G. Ruan, Z. Yan, D. Natelson, J. M. Tour, ACS Nano 2013, 7, 6001-6006.

14. S. J. Ding, J. S. Chen, X. W. Lou, Adv. Funct. Mater. 2011, 21, 4120.

15. Q. Wang, X. Wang, B. Liu, G. Yu, X. Hou, D. Chen, G. Shen, J. Mater. Chem. A 2013, 1, 2468-2473.

16. S. Bai, X. Shen, X. Zhong, Y. Liu, G. Zhu, X. Xu, K. Chen, Carbon 2012, 50, 2337.

17. J. W. Xiao and S. H. Yang, RSC Adv. 2011, 1, 588–595.

18. X. D. Zhang, Z. S. Wu, J. Zang, D. Li, Z. D. Zhang, J. Phys. Chem. Solids 2007, 68, 1583-1590.

19. P. Ahuja, S. K. Ujjain, R.K Sharma and G. Singh, RSC Advances DOI: 2014, c4ra09027f.

20. Y.Liu, Y.Wang, X.Xu, P.Sun, T.Chen, RSC Adv. 2013, DOI: 10.1039/C3RA47065B.

21. G. Zhang , L. Yu , H. B. Wu , H. E. Hoster, X. W. (David) Lou, Adv. Mater. 2012, 24, 4609–4613.

22. G. T. Bhandaget, H. V. Keer, J. Phys. C: Solid State Phys. 1978, 11, L219-L221.

23. Y. Qiu, Y. Zhao, X. Yang, W. Li, Z. Wei, J. Xiao, S. F. Leung, Q. Lin, H. Wu, Y. Zhang, Z. Fan, S. Yang, Nanoscale 2014, 6, 3626-3631.

24. L. Deng, G. Zhu, J. Wang, L. Kang, Z. H. Liu, Z. Yang, Z. Wang, J. Power Sources 2011, 196, 10782-10787.

25. L. Yuan, X. H. Lu, X. Xiao, T. Zhai, J. Dai, F. Zhang, B. Hu, X. Wang, L. Gong, J. Chen, C. Hu, Y. Tong, J. Zhou, Z. L. Wang, ACS Nano 2012, 6, 656-661.

26. M. Egashira, H. Todo, N. Yoshimoto, M. Morita, J. Power Sources 2008, 178, 729-735.

27. D. Bansal, F. Cassel, F. Croce, H. Hendrickson, E. Plichta, M. Salomon, J. Phys. Chem. B 2005, 109, 4492-4496.

28. P. Ahuja, V. Sahu, S. K. Ujjain, R. K. Sharma, G. Singh, Electrochim. Acta 2014, 146, 429–436

29. R. K. Sharma, H. S. Oh, Y. G. Shul, H. Kim, J. Power Sources 2007, 173, 1024-1028.

30. G. P. Pandey, A.C. Rastogi, J. Electrochem. Soc. 2012, 159, A1664-A1671.

31. S. K. Ujjain, K. Deori, R. K. Sharma, S. Deka, ACS Appl. Mater. Interfaces 2013, 5, 10665-106672.

32. J. Zhang, Z. Xiong, X. S. Zhao, J. Mater. Chem. A2011, 21, 3634-3640.

33. J. Yan, Z. Fan, W. Sun, G. Ning, T. Wei, Q. Zhang, R. Zhang, L. Zhi, F. Wei, Adv. Funct. Mater. 2012, 22, 2632-2641.

34. L. Wang, X. Wang, X. Xiao, F. Xu, Y. Sun, Z. Li, Electrochim. Acta 2013, 111, 937-945.

35. A. C. Ferrari, J. C. Meyer, V. Scardaci, C Casirashi, M. Lazzeri, F. Mauri, S. Piscanec, D. Jiang, K. S. Novoselov, S. Roth, A. K. Geim, Phys. Rev. Lett. 2006, 97, 187401.

36. S. Stankovich, D. A. Dikin, R. D. Piner, K. A. Kohlhaans, A. Kleinhammes, Y. Y. Jia, Y. Wu, S. T. Nguyan, R. S. Ruoff, Carbon 2007, 45, 1558.

37. S. Guo, D. Wen, Y. Zhai, S. Dong, E. Wang, ACS Nano 2010, 4, 3959.

38. H. Li, B. Song, W. J. Wang, X. L. Chen, Mat. Chem. Phys. 2011, 130, 39-44.

39. X Zhao, H Lin, J Li, L Xin, C Liu, J Li, Carbon 2012, 50, 3497-3502.

40. P. Zhang, X. Li, Q. Zhao, S. Liu, Nanoscale Res. Lett. 2011, 6, 323-331.

41. J. Zheng, S. S. Moganty, P. C. Goonetilleke, R. E. Baltus, D. Roy, J. Phys. Chem. C 2011, 115, 7527-7537.

42. R. B. Rakhi, W.Chen, H. N. Alshareef, Nano Lett. 2012, 12, 2559-2567.

43. Y. He, W. Chen, X. Li, Z. Zhang, J. Fu, C. Zhao, E. Xie, ACS Nano, 2013, 7, 174-182.

44. R. S. Hastak, P. Sivaraman, D. D. Potphode, K. Shashidhara, A. B. Samui, J. Solid State Electrochem. 2012, 16, 3215-3226.

45. M. F. El-Kady, V. Strong, S. Dubin, R. B. Kaner, Science 2012, 335, 1326-1330.

46. C. Ramasamey, J. P. Del Val, M. Anderson, J. Power Sources 2014, 248, 370-377.

47. K. Naoi, K. Ueyama, T. Osaka, W. H. Smyrl, J. Electrochem. Soc. 1990, 137, 494-499.

48. S. K. Ujjain, A. Das, G. Srivastava, P. Ahuja, M. Roy, A. Arya, K. Bhargava, N. Sethy, S. K. Singh, R. K. Sharma, M. Das, Biointerphases 2014, DOI: 10.1116/1.4890473.

49. V. Ganesh, S. Pitchumani, V. Lakshminarayanan, J Power Sources 2006, 158, 1523-1532.

50. Z. Lei, Z. Liu, H. Wang, X. Sun, L. Lu, X. S. Zhao, J. Mater. Chem. A 2013, 1, 2313-2321

Figure Captions

Figure 1 (a) TEM micrograph of $ZnMn_2O_4$/GNR, large area distribution of $ZnMn_2O_4$/GNR, arrow demarcate the individual $ZnMn_2O_4$/GNR (b) $ZnMn_2O_4$/GNR with magnified image, inset shows the mono-dispersivity, (b) HRTEM of $ZnMn_2O_4$/GNR, (c) Spotty SAED pattern of $ZnMn_2O_4$/GNR, (f) SEM micrograph of $ZnMn_2O_4$/GNR film and (e) X-ray diffraction patterns of $ZnMn_2O_4$/GNR and GONR.

Figure 2 (a) Raman spectra and (b) FTIR spectra of $ZnMn_2O_4$/GNR and GONR.

Figure 3 (a) Cyclic voltammograms (CV) of $ZnMn_2O_4$/GNR||$ZnMn_2O_4$/GNR in different potential range at 25 mVs^{-1}, inset shows capacitance variation with cell voltage, (b) CV of GNR||GNR, $ZnMn_2O_4$||ZnMn2O4 and $ZnMn_2O_4$/GNR|| $ZnMn_2O_4$/GNR at 25 mVs^{-1}, (c) CV of $ZnMn_2O_4$/GNR||$ZnMn_2O_4$/GNR at different scan rates, inset shows rate capability curve of the cell and (d) CV of $ZnMn_2O_4$/GNR||$ZnMn_2O_4$/GNR cell at 80mVs^{-1} as a function of temperature.

Figure 4(a) Nyquist plot of $ZnMn_2O_4$/GNR||$ZnMn_2O_4$/GNR at 25^oC and 75^oC in frequency range 1m Hz-1MHz. Inset shows high frequency region, (b) Plot of |Z| vs $\omega^{-1/2}$ for calculating diffusion coefficient at 25^oC and 75^oC, Variation of active and reactive power with change in frequency at (c) 25^oC and (d) 75^oC.

Figure 5 (a) GCD of GNR||GNR, $ZnMn_2O_4$||$ZnMn_2O_4$ and $ZnMn_2O_4$/GNR||$ZnMn_2O_4$/GNR at 1.25 Ag^{-1}, (b) GCD of $ZnMn_2O_4$/GNR||$ZnMn_2O_4$/GNR at different current density, (c) Ragone plot and (d) Cycling life test of $ZnMn_2O_4$/GNR||$ZnMn_2O_4$/GNR with charge/discharge profile in inset.

Figure 6 GCD cycling of $ZnMn_2O_4$/GNR||$ZnMn_2O_4$/GNR at 0.2 Ag^{-1} under normal, bent and twisted state with corresponding photograph in inset. Second inset shows GCD curves of the cell under different conditions.

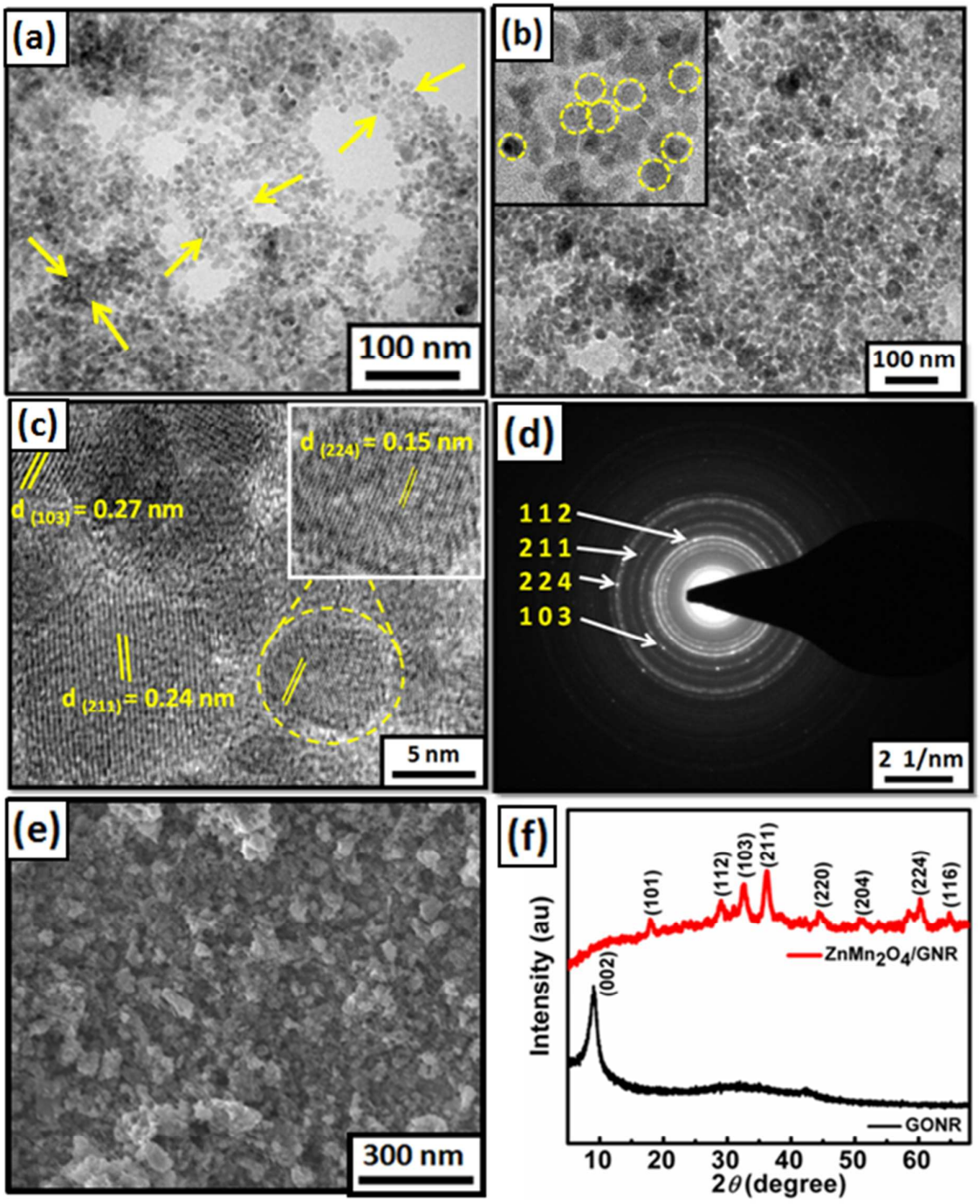

Figure 1

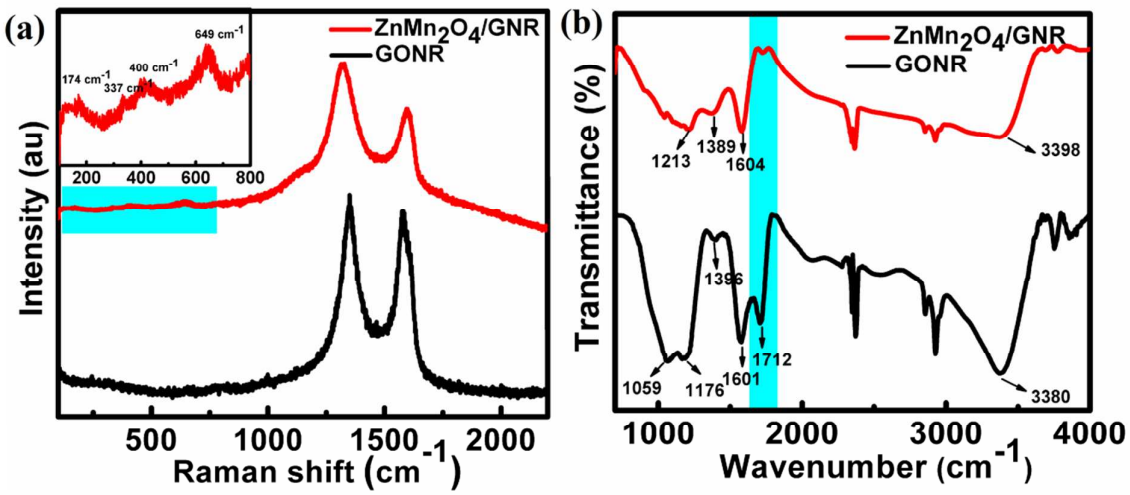

Figure 2

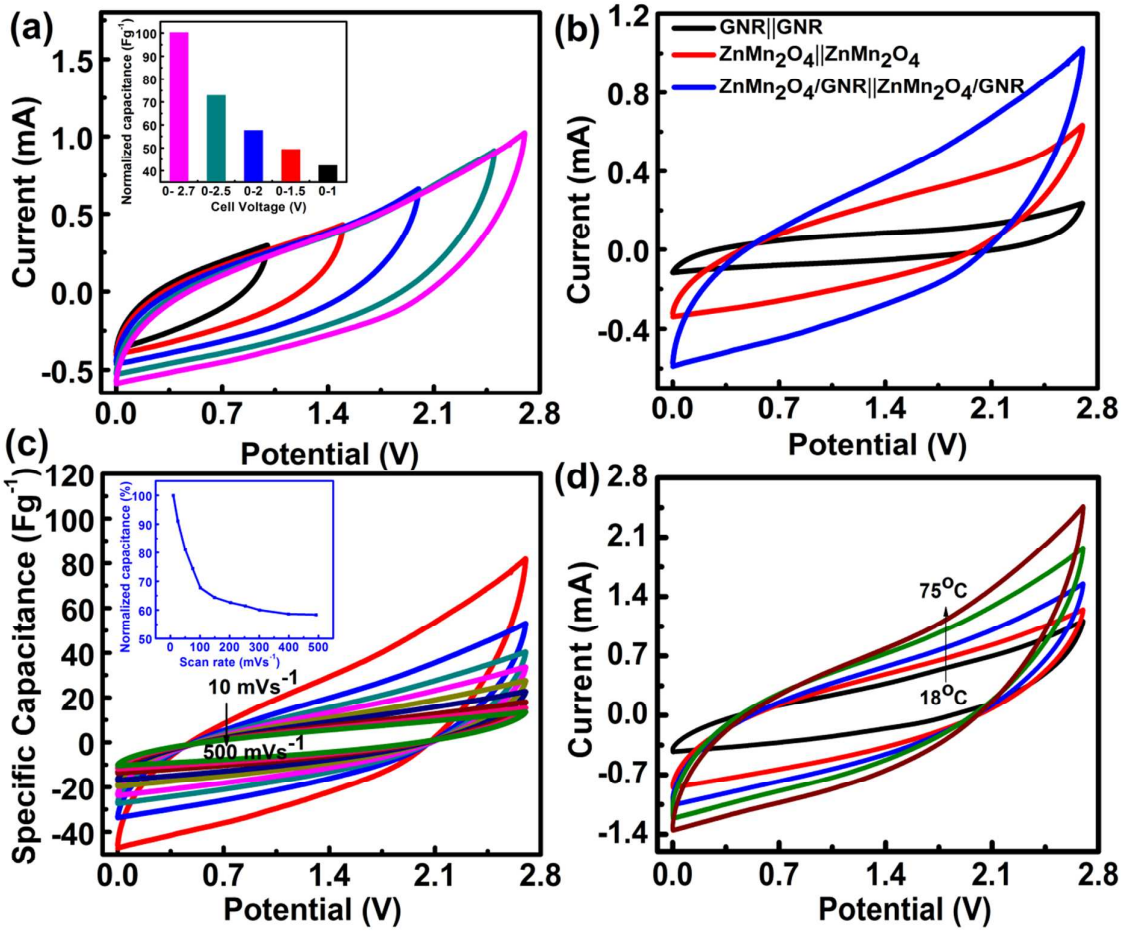

Figure 3

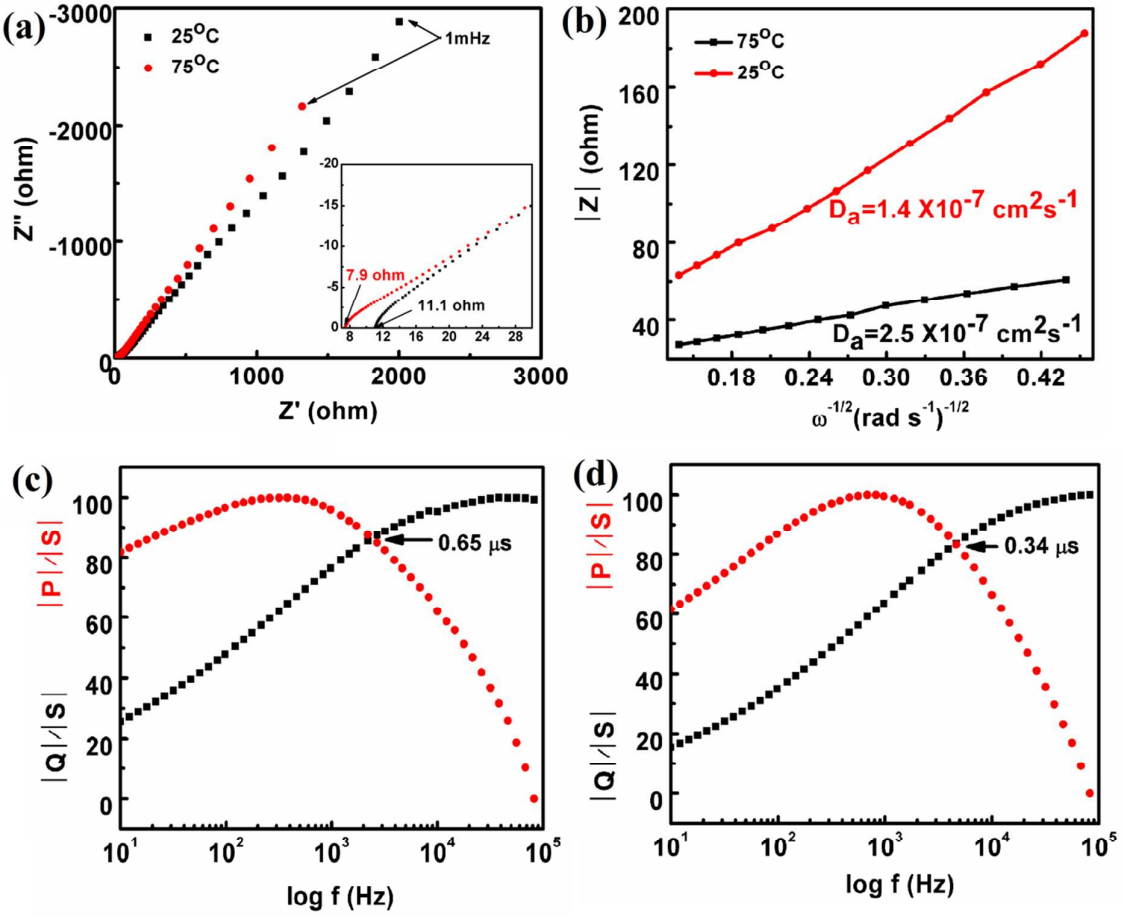

Figure 4

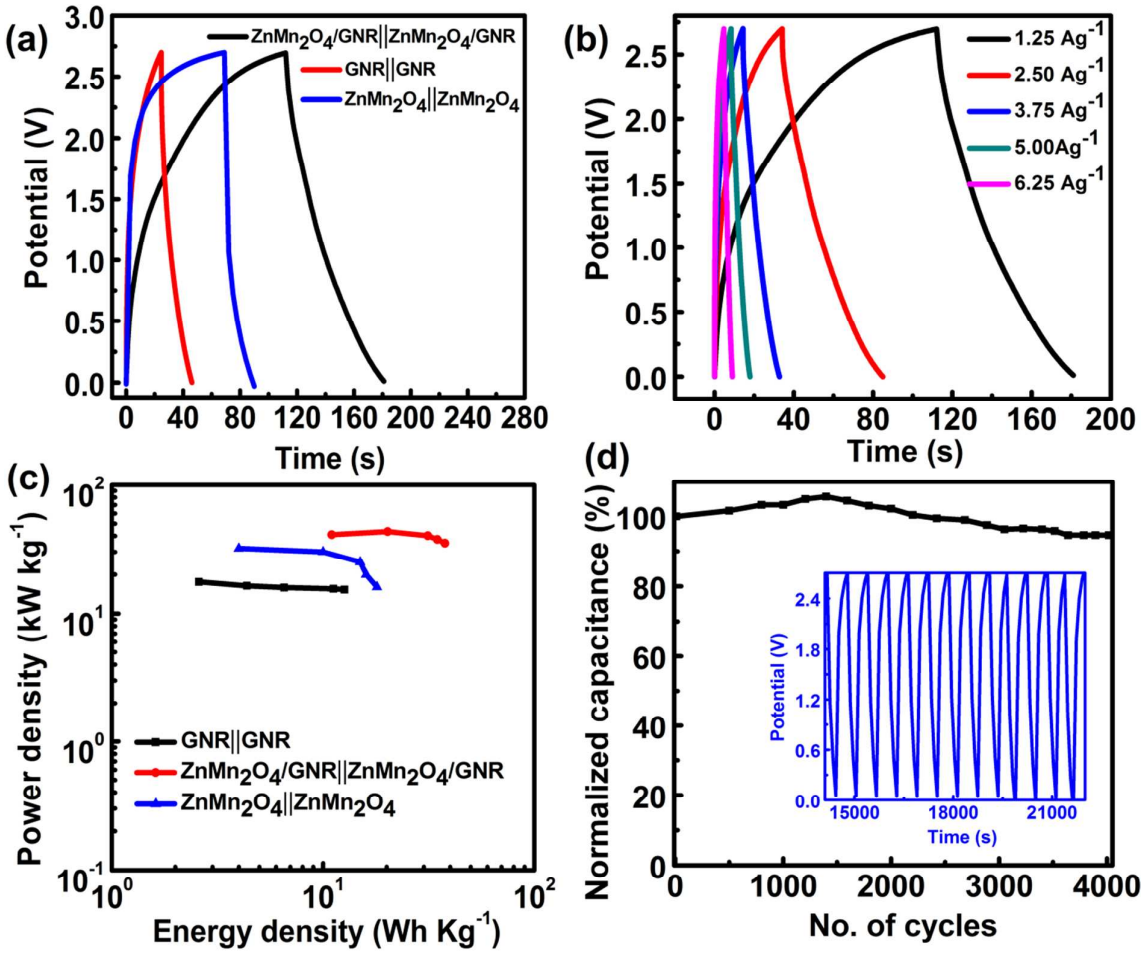

Figure 5

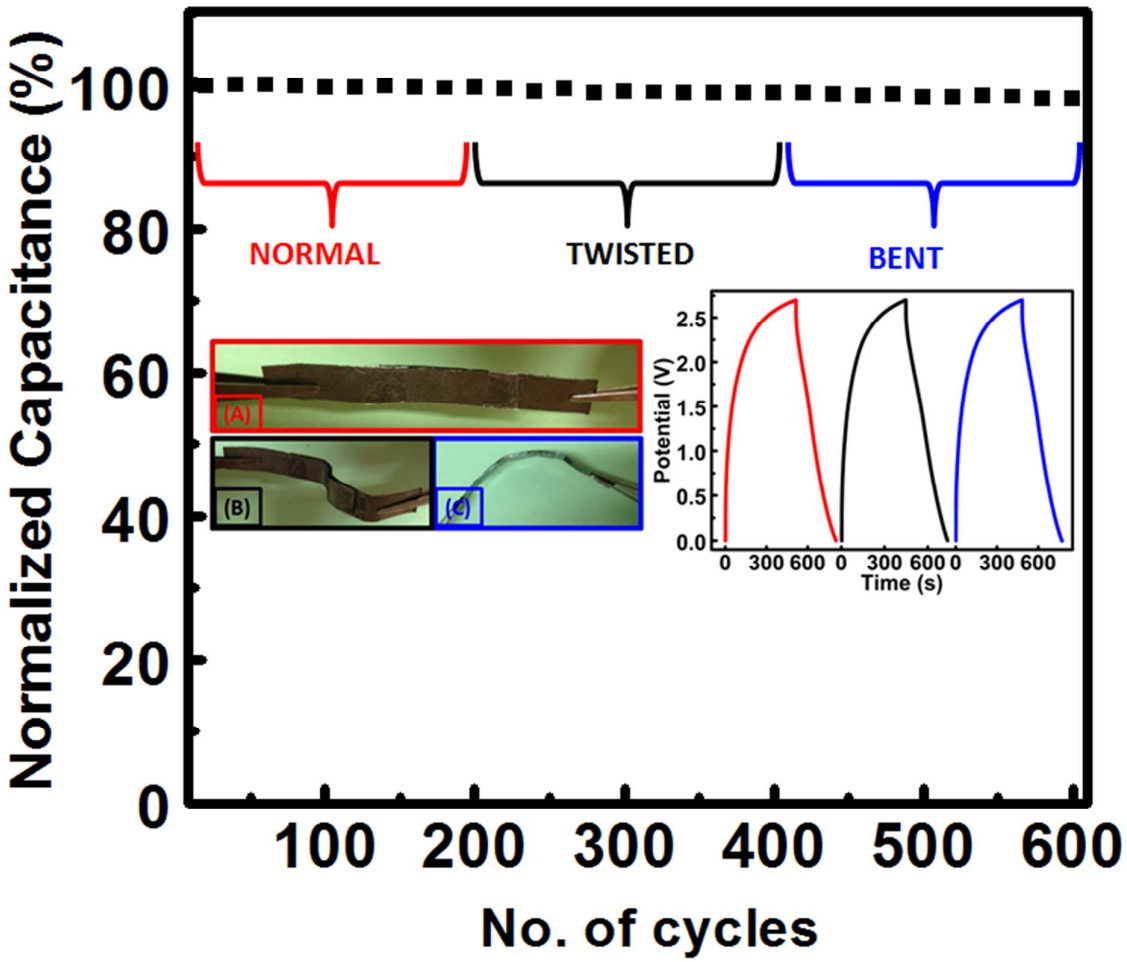

Figure 6

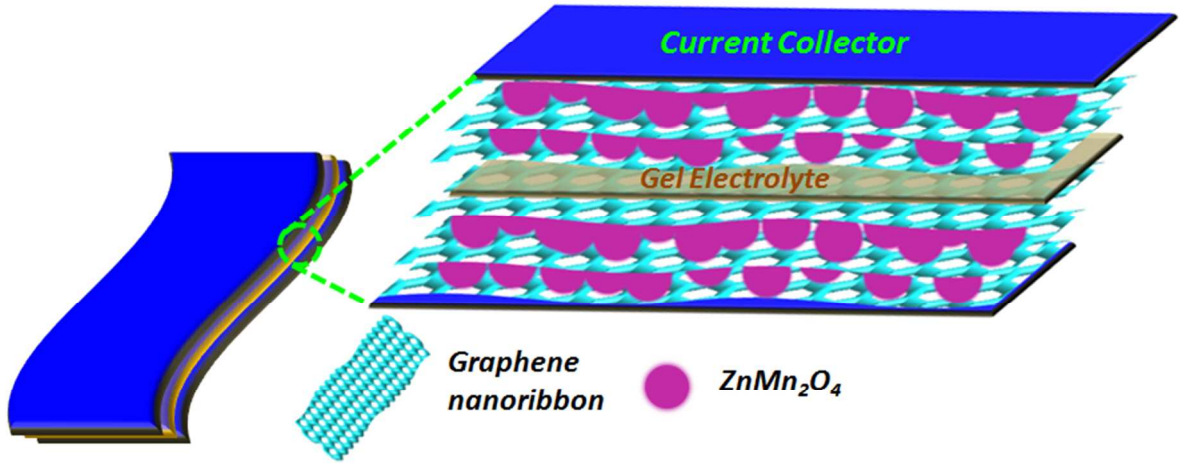

Graphical Abstract